

## EXPECTED EMISSION FROM MERCURY'S EXOSPHERIC SPECIES, AND THEIR ULTRAVIOLET-VISIBLE SIGNATURES

R. KILLEN<sup>1</sup>, D. SHEMANSKY<sup>2</sup>, AND N. MOUAWAD<sup>1</sup>

<sup>1</sup> Department of Astronomy, University of Maryland, College Park, MD 20742, USA; r.killen@astro.umd.edu, mouawad@astro.umd.edu

<sup>2</sup> Space Environment Technologies, Planetary and Space Science Division, Pasadena, CA 91107, USA; dshemansky@spacenvironment.net

Received 2008 September 1; accepted 2009 January 21; published 2009 March 11

### ABSTRACT

Solar photon scattering probabilities ( $g$  values) have been calculated for discrete transitions in 12 species, in a format designed primarily to allow analysis of spacecraft observations from *MESSENGER* and *BepiColombo* at Mercury. The results support observations using the *MESSENGER* Ultraviolet and Visible Spectrometer spectrograph experiment operating over the spectral range 1150–6000 Å and the *BepiColombo* spectrograph in the range 550–3150 Å. Significant radial velocity dependence is shown for most of the emission lines, a critical factor for interpretation of the observed spectra. The  $g$  values have general application for solar system emission sources dominated by scattering of the solar flux.

*Key words:* atomic data – radiation mechanisms: general – ultraviolet: solar system

*Online-only material:* machine-readable tables

### 1. INTRODUCTION

The discrete photoemission properties of atomic and molecular species stimulated by solar radiation are an important tool for quantitative work with remote sensing experiments. In an optically thin atmosphere, the total column amount of a given species is given in terms of a solar-forced  $g$  value defined as an emission probability per atom ( $\text{photons s}^{-1} \text{atom}^{-1}$ ). For an optically thin gas and a measured emission brightness  $I$ , abundance  $N$  is obtained through the relation  $N \propto I/g$ .

The solar discrete emission spectrum in the extreme-ultraviolet/far-ultraviolet (EUV/FUV) and Fraunhofer spectrum at longer wavelengths are responsible for strong dependence of the  $g$  values on Doppler velocity for many species. Because of Mercury's eccentric orbit, some  $g$  values can vary by over an order of magnitude during the orbital period. Thus, knowledge of how the  $g$  values vary is critical to the interpretation of spectroscopic data. In addition to variation with Doppler shift, we have considered variation with an assumed gas temperature. In this work,  $g$  values have been calculated for 12 species that will be targeted by *MESSENGER* and/or *BepiColombo*. The Ultraviolet and Visible Spectrometer (UVVS) channel on *MESSENGER*'s Mercury Atmospheric and Surface Composition Spectrometer (MASCS) is a scanning grating monochromator that covers the wavelength range 1150–6100 Å with an average 6 Å spectral resolution (McClintock & Lankton 2007). The *BepiColombo* UV spectrometer, PHEBUS, is a double spectrometer for the EUV range (550–1550 Å) and the FUV range (1450–3150 Å) using two Micro Channel Plate (MCP) detectors with a spectral resolution of 1 nm for the EUV range and 1.5 nm for the FUV range (Chassefiere & The PHEBUS Team 2009).

Species of interest include sodium, potassium, and calcium, which have been observed in Mercury's exosphere through ground-based observations, and hydrogen and oxygen, measured by the UV spectrometer experiment on the Mariner 10 spacecraft. In addition, sulfur, magnesium, carbon,  $\text{Ca}^+$ , and  $\text{Mg}^+$  have emission lines in the UV that are observable by the *MESSENGER* UVVS as well as *BepiColombo*. Helium EUV emission at 584 Å will be observable by the *BepiColombo* UV

spectrometer. Of particular importance for Mercury is the dependence of the  $g$  values on the bulk motion of the gas relative to the Sun. These quantities are applicable to other astronomical observations where emission is forced by solar radiation.

### 2. METHOD

This section provides a description of the physical relationships and limits to the determination of the emission probability for solar-forced fluorescence. The physical considerations involved in the calculation of photon scattering probabilities are discussed by Mitchell & Zemansky (1971, Chap. III, V). Chamberlain (1961, p. 424) provides a definition of the  $g$  value, but the formulation is not general and does not account for radiationless deactivation, the distribution of population in states of the excited species, or the kinetic temperature of the fluorescent volume. The present model calculations are unique in intrinsically including all of the latter effects. The present model calculations, however, assume isotropic scattering, and do not address polarization effects or scattering phase function as discussed by Chamberlain (1961, Section 11.1.2) and Mitchell & Zemansky (1971, Chap. V). Generalization of the  $g$ -value definition occurs in the literature where, for example, the quantity refers to the partitioning of products in photochemistry (see Elliot et al. 1990). The core quantity for a given species is the volumetric excitation rate of the state  $j$ ,  $\mathcal{G}_{ij}$ , given by

$$\mathcal{G}_{ij} = \int \pi \mathcal{F}_\nu \cdot \frac{r_0^2}{r^2} \cdot k_v^{ij} d\nu \quad (1)$$

in units of  $n_j \text{ cm}^{-3} \text{ s}^{-2}$ , where  $n_j$  is the population of state  $j$ ,  $\pi \mathcal{F}_\nu$  is the differential solar flux at 1 AU in units of photons  $\text{cm}^{-2} \text{ s}^{-1} (\text{cm}^{-1})^{-1}$ ,  $r_0$  is 1 AU, and  $r$  is the distance of the gas volume from the Sun.  $k_v^{ij}$  is the absorption coefficient ( $\text{cm}^{-1}$ ) for the  $i \rightarrow j$  transition, and  $\nu$  is the wavenumber ( $\text{cm}^{-1}$ ).

The core of the absorption line is dominated by the kinetic energy distribution of the atoms, and for this reason a Doppler line shape is utilized for practical single scattering calculations.

The absorption coefficient for a given transition is

$$k_v^{ij} = k_o^{ij} \exp\left(-\left[\frac{v - v_o}{\alpha_v} \cdot 2 \cdot (\ln 2)^{1/2}\right]^2\right), \quad (2)$$

where  $k_o^{ij}$  is the absorption coefficient at line center, and  $v_o$  is the line center wavenumber.  $\alpha_v$ , the Doppler line FWHM ( $\text{cm}^{-1}$ ), is given by

$$\alpha_v = \frac{(2)(2 \ln 2)^{1/2}}{c} v_o \left(\frac{kT}{m}\right)^{1/2}, \quad (3)$$

where  $k$  is the Boltzmann constant,  $c$  is the speed of light, and  $m$  is the atomic mass. The line strength,  $S^{ij}$ , is given by

$$S^{ij} = \int k_v^{ij} dv = h\nu B_{ij} N_i \quad (4)$$

in units of  $\text{cm}^{-2}$ , where  $N_i$  is the density of the gas in state  $i$ ,  $h$  is Plank's constant, and  $B_{ij}$  is the Einstein absorption probability in radiation density units.

Quantities at line center needed for the calculation of Equation (1) are

$$k_o^{ij} = \frac{S^{ij}}{\alpha_v} \cdot 2 \cdot \left(\frac{\ln 2}{\pi}\right)^{1/2}, \quad (5)$$

$$\sigma_o^{ij} = \frac{k_o^{ij}}{N_i}, \quad (6)$$

$$\sigma_o^{ij} = \left(\frac{2}{\alpha_v}\right) \left(\frac{\ln 2}{\pi}\right)^{1/2} h\nu_o B_{ij}, \quad (7)$$

$$\tau_o^{ij} = k_o^{ij} \cdot \ell = \sigma_o \cdot N_i \cdot \ell. \quad (8)$$

Here,  $\ell$  is the effective line-of-sight path length, and  $\sigma_o^{ij}$  is the absorption cross section at line center. The optical depth,  $\tau_o^{ij}$ , should be less than 0.2 in order to retain a good approximation to calculated abundances.

The rate  $\mathcal{G}_{ij}$  defined in Equation (1), supplying population to state  $j$ , must then be distributed among the total number of states in the excited species in a radiative/collisional equilibrium in order to determine emission efficiencies from the species. Although in many species activated by the deposition of energy most of the population lies in the ground state, there are a significant number of cases in which excited states contain a measurable fraction of the total population. Accurate calculations cannot assume all of the population of a species to be in the ground state. It is therefore necessary to calculate the steady-state populations of all significant states of a species excited under the anticipated conditions. If the species contains long-lived metastable states (such as atomic nitrogen) the time constant for reaching equilibrium may have to be considered. The prediction of accurate emission efficiencies then requires that the entire emission spectrum of the species be calculated. A generally applicable formulation for model calculations applied to this purpose developed by Shemansky (1980) and Shemansky & Smith (1981) and subsequent generations (COREQ50) is applied here using species state architectures developed over time within

Shemansky's research program, and updated as more accurate fundamental physical parameters became available. Many transition probabilities have been obtained from the NIST archive (Ralchenko et al. 2008), but a number of other experimental and theoretical sources have been incorporated including in-house values calculated using the Coulomb approximation (Bates & Damgaard 1949, see Klarsfeld 1988). The model calculations establish the populations for all states of a species,  $N_i$ , excited by the combined forcing of solar flux and assumed dual populations of Maxwellian electrons, one representing an ambient population  $e_a$ , and one a forcing electron population,  $e_s$ , responsible for maintaining  $e_a$ . The density and temperature of  $e_a$  and  $e_s$  are nominal (in all cases the state of the gas is dominantly determined by solar forcing) and have little effect except to cause relaxation in the fine structure of the ground state of some species. The model calculation establishes the internal non-LTE state of the atom, but is fully intrinsically bound by the Principle of Detailed Balance (Condon & Shortley 1959). The model calculation produces predicted volumetric emission rates,  $\mathcal{I}_{ji}$ , from the calculated  $N_j$ ,

$$\mathcal{I}_{ji} = N_j \cdot A_{ji}, \quad (9)$$

$$N = \sum_i N_i, \quad (10)$$

$$g_{ji} = \frac{\mathcal{I}_{ji}}{N}, \quad (11)$$

where  $A_{ji}$  is the transition probability counterpart of  $B_{ij}$ . The abundance of gas from observed emission lines of spatially extended sources is then obtained from the  $g$  value using the relation

$$N \cdot \ell = \frac{\mathcal{I}_B^{ji} \times 10^6}{g_{ji}}, \quad (12)$$

where  $\mathcal{I}_B^{ji}$  is the measured brightness in Rayleighs.

The Maxwellian kinetic distribution assumed here is only approximate at Mercury. The discrete solar lines cause  $g$ -value sensitivity to gas bulk velocity relative to the Sun (Equation (1)). Mercury's radial velocity varies approximately between  $-10$  and  $+10 \text{ km s}^{-1}$ . The component of bulk motion of the gas along the line to the Sun shifts the wavelength of the impacting solar flux according to

$$v_D = \frac{dr}{dt}, \quad (13)$$

$$\lambda_D = \frac{\lambda_0}{(1 - \frac{v_D}{c})}, \quad (14)$$

where  $v_D$  is the radial velocity component,  $r$  is the range to the Sun,  $\lambda_0$  is the rest-frame solar spectrum wavelength,  $\lambda_D$  is the Doppler-shifted wavelength of the impacting solar flux, and  $c$  is the speed of light. A negative  $v_D$  increases the frequency of the impacting flux and shortens the wavelength of the solar spectrum at the absorbing gas volume.

The solar flux in the present calculation is a mean at solar minimum (machinereadable tables available online). Solar flux

**Table 1**  
 $g$  Values for the Strong Lines Targeted in Mercury's Atmosphere, Gas Temperatures, and Masses Assumed in the Calculations of  $g$  Values

Species	Gas Temperature (K)	Mass (amu)	Vacuum Wavelength (Å)	$g$ Value at M1 ( $R = 0.35$ AU and $V_D = -10$ km s $^{-1}$ ) (ph atom $^{-1}$ s $^{-1}$ )	$g$ Value ( $r = 0.47$ AU and $V_D = 0$ km s $^{-1}$ ) (ph atom $^{-1}$ s $^{-1}$ )
H I	450	1.00	(1215.7) <sup>a</sup>	1.26E-02	0.67E-02
He I	565	4.00	584.4	3.79E-05	2.63E-05
C I	12,000	12.01	(1657.2) <sup>a</sup> (1560.8) <sup>a</sup>	2.98E-04 0.70E-04	1.55E-04 0.40E-04
O I	12,000	16.00	1302.2 1304.9 1306.0	6.16E-05 3.67E-05 1.23E-05	3.24E-05 1.93E-05 6.50E-06
Na I	1200	22.99	5891.6 5897.6 3303.3 3303.9	3.84E+01 2.33E+01 5.52E-02 2.47E-02	2.38E+00 1.39E+00 2.45E-03 2.65E-03
K I	1200	39.10	4045.2 4048.4	5.21E-02 2.28E-02	2.45E-02 1.25E-02
Ca I	3000	40.09	4227.9 4576.7 2722.5	2.25E+01 1.21E-01 2.36E-02	2.43E+00 1.87E-02 5.91E-03
Ca II	3000	40.09	3934.8 3969.6	2.87E+00 0.82E+00	1.15E+00 0.31E+00
Mg I	12,000	24.30	2853.0 2026.5	3.41E-01 1.71E-03	1.50E-01 1.01E-03
Mg II	3000	24.30	2796.4 2803.5	6.42E-01 3.80E-01	3.69E-01 1.71E-01
S I	3000	32.06	1807.3 1820.3 1826.2	3.00E-04 1.61E-04 5.35E-05	1.69E-04 9.03E-05 3.00E-05
OH	3000	17.00	(3081) <sup>a</sup> (3092) <sup>a</sup>	3.50E-04 2.37E-04	1.50E-04 1.12E-04

**Note.** <sup>a</sup>Bracketed wavelengths,  $\langle \rangle$ , signs indicate post-model multiple transition summation.

variability will affect the values given here in the FUV, and corrections can be made by scaling to the flux data given here. The solar UV flux has been monitored for the past three decades, and is available online at the LISIRD Web site maintained by the University of Colorado (Snow & The LISIRD Team 2005).

### 3. RESULTS

$g$  values were calculated for 12 species (H, He, C, O, Na, K, Mg, Mg II, S, Ca, Ca II, OH) using the Collisional Radiative Equilibrium (COREQ50) model. The strongest lines are listed in Table 1 for the region 550–6000 Å,  $r = 0.352$  AU, and 0.47 AU (aphelion). The assumed electron populations are given by electron density,  $e_a = 10^3$  cm $^{-3}$ , at temperature,  $T_a = 1000$  K, and  $e_s = 1.0$  cm $^{-3}$  at  $T_s = 3 \times 10^5$  K. The effect of the forcing electrons,  $e_s$ , on emission efficiency is small. The ambient electron density is a crude estimate of physical reality, and the main effect is to cause relaxation in multiplet ground states. The solar flux model used in the calculations contains a combination of calculated and measured high-resolution line shapes with pixel widths of 2 mÅ resolution in the EUV/FUV and 5 mÅ at longer wavelengths (machinereadable tables available online). The solar spectrum is corrected for Earth extinction effects at the strong resonance lines of sodium and potassium.

Table 2 provides optical depth information, Figure 1 plots  $g$  values for a single radial velocity, Figures 2–13 give  $g$  values at a single radial distance as a function of radial velocity, Figures 15–17 give  $g$  values as a function of true anomaly angle, and Table A1 gives the first few lines of the solar flux model, shown in full in the online journal. Wavelengths are given in

vacuum.  $g$ -Value plots are given as a function of the heliocentric radial velocity of the atom between  $-12$  km s $^{-1}$  and  $+12$  km s $^{-1}$  at a distance,  $r$ , of 0.352 AU for the strongest lines. The radial velocity of Mercury with respect to the Sun is a function of true anomaly angle.

In some cases, bulk velocity of the target gas may not be the same as the planet radial velocity. Table 1 also gives the gas temperature ( $T_g$ ) and the atomic mass (amu) used in the calculation.

The temperatures ( $T_g$ ) for H I and He I were estimated from scale heights measured by the Mariner 10 UVVS (Broadfoot et al. 1976). The temperatures for Na I and Ca I are estimated from ground-based measured line profiles (Killen et al. 1999, 2005). Refractory species, such as Mg I, are assumed to be hot since their ejection mechanism is most likely sputtering by ions (Wurz et al. 2007). O I is assumed to be hot since atomic oxygen may be produced as a result of dissociation of an oxide (Killen et al. 2005). The oxygen scale height was not measured by Mariner 10, but the abundance is consistent with an escaping oxygen exosphere or corona (Killen et al. 2005).

#### 3.1. Discussion

The single scattering relationships break down seriously for the sodium atmosphere at Mercury. The sodium D2 line for line-of-sight column greater than about  $3 \times 10^{10}$  atoms cm $^{-2}$  (Table 2) is optically thick. Given that the absorption coefficient at line center is a function of the line profile, the optical depth at line center is a function of the temperature of the gas (Equations (3) and (7)). Table 2 gives the line-of-sight column abundance in atoms cm $^{-2}$  at which the optical depth is unity and 0.2, respectively. Optical depth unity is often stated as “optically thick,” thus both values are given in the table.

**Table 2**  
Column Abundances for  $\tau = 1$  and 0.2

Species	$\lambda$ (nm)	( $\tau = 1$ )	( $\tau = 0.2$ )
Na	589.1580	0.16450E+12	0.32900E+11
Na	589.7550	0.32918E+12	0.65836E+11
Na	330.3327	0.20896E+14	0.41792E+13
Na	330.3941	0.42159E+14	0.84317E+13
Mg	285.2960	0.37449E+12	0.74899E+11
Mg	202.6480	0.83983E+13	0.16797E+13
H	121.5670	0.36077E+13	0.72153E+12
O	130.2170	0.17392E+14	0.34785E+13
O	130.4850	0.17424E+14	0.34847E+13
O	130.6030	0.17374E+14	0.34749E+13
K	404.5240	0.19397E+14	0.38794E+13
K	404.8360	0.38637E+14	0.77275E+13
C	165.7000	0.27175E+14	0.54350E+13
C	156.1400	0.32317E+14	0.64633E+13
Ca	422.7920	0.10067E+12	0.20134E+11
Ca	272.2450	0.30399E+15	0.60798E+14
He	58.77400	0.28557E+12	0.57115E+11
Mg II	279.6350	0.56557E+12	0.11311E+12
Mg II	280.3530	0.11320E+13	0.22639E+12
S	180.7310	0.41888E+13	0.83776E+12
S	182.0340	0.41588E+13	0.83176E+12

Optical depth is given by Equation (8).  $g$  values for strong resonant emission lines have strong dependence on radial velocity because of the solar spectral structure as stated above. The sodium D lines at 5891.6 Å and 5897.6 Å vary by an order of magnitude, and the Ca I line at 4227 Å varies by a factor of  $\sim 6$  from zero to  $\pm 10$  km s<sup>-1</sup> radial velocity. The  $g$  values for some lines are highly asymmetric with respect to positive and negative radial velocity due to the asymmetry in the underlying solar spectrum [e.g., K I (4045, 4048 Å), S I (1807 Å), Mg I (2052 Å), and Mg II (2796, 2803 Å)]. There is little radial velocity dependence in the  $g$  value for the Ly $\alpha$  line (1215 Å)

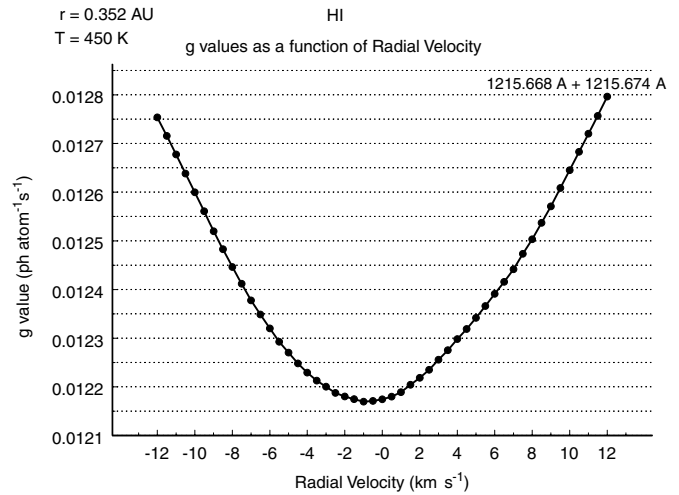


**Figure 2.** Variation in  $g$  value for the H Ly $\alpha$  line is given as a function of radial velocity,  $v_D$ , for  $r = 0.352$  AU. Similar plots are also shown for the other species in Figures 3–14. True anomaly angle dependence is given in Figures 15–18.

because of extreme optical thickness in the solar line. There are known cases in which the gas volume has a radial velocity differing significantly from that of the parent planetary body (Potter et al. 2007). A moderate dependence on gas temperature for some species is evident.

Variability of the sodium D lines with Doppler shift was previously considered by Brown & Yung (1976), but a systematic study of  $g$ -value variability has not been undertaken previously. A maximum of 20% variation is seen in the  $g$  value for the 3081 Å OH band while changing temperature between 3000 and 15,000 K, thus the uncertainty in gas temperature is not critical to the interpretation. Optical depth effects are probably not important for any of the species considered except for the Na D lines and the Mg 2853 Å line. These lines are strong, and

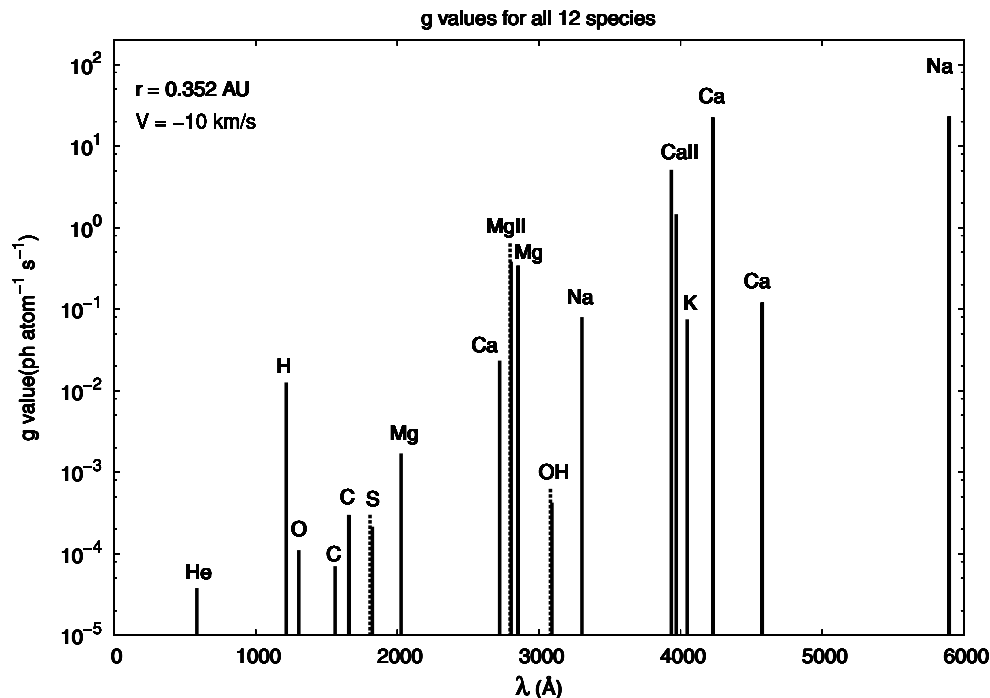


**Figure 1.**  $g$  values for  $r = 0.352$  AU and  $v_D = -10$  km s<sup>-1</sup> for 12 species' selected transitions lines in the 500–6000 Å region.

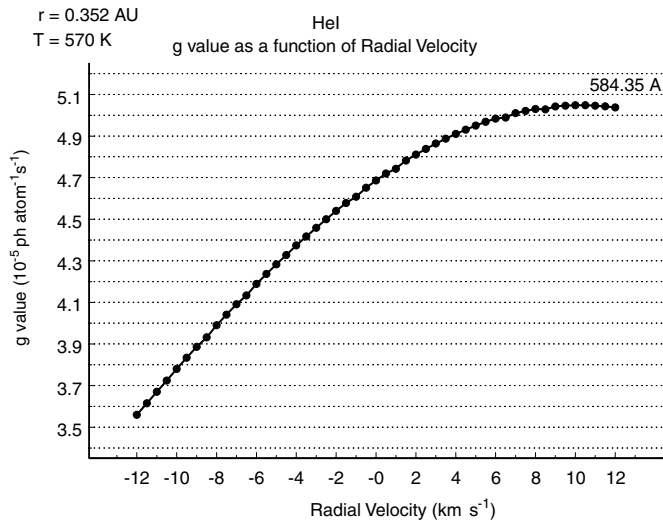


**Figure 3.**  $g$  value for the 584 Å spectral line for He is shown as a function of radial velocity for  $r = 0.352$  AU. The calculation is for a gas temperature of 565 K, consistent with results from the Mariner 10 UVVS observations.

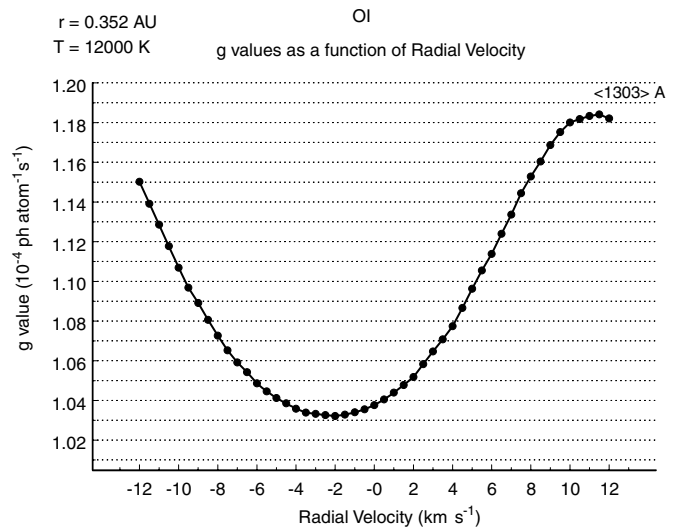


**Figure 5.**  $g$  value is shown as a function of heliocentric radial velocity for the O I (1303) Å triplet; <1303> Å is the mean wavelength of the oxygen triplet lines (see Table 1). The high temperature ( $T_g$ ) is consistent with a two-stage process for the production of oxygen as a dissociation product of an oxide (e.g., Killen et al. 2005).

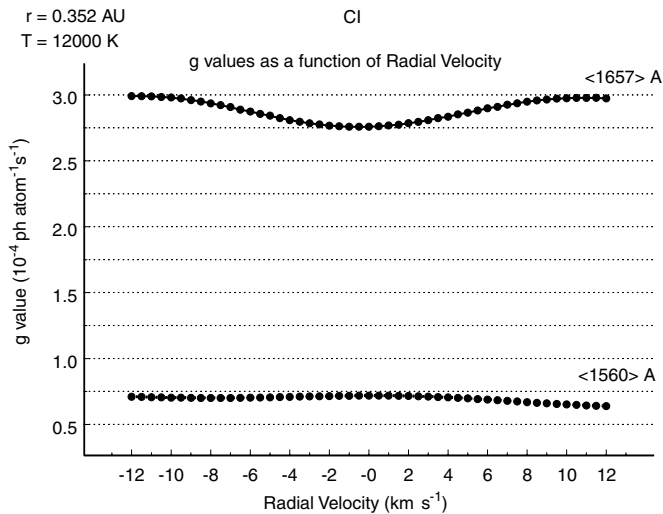


**Figure 4.**  $g$  values for carbon emission lines in the 1500–1600 Å range are shown vs. heliocentric radial velocity for  $r = 0.352$  AU at an assumed temperature of 12,000 K, and range of heliocentric velocities of  $\pm 12$  km  $s^{-1}$ .

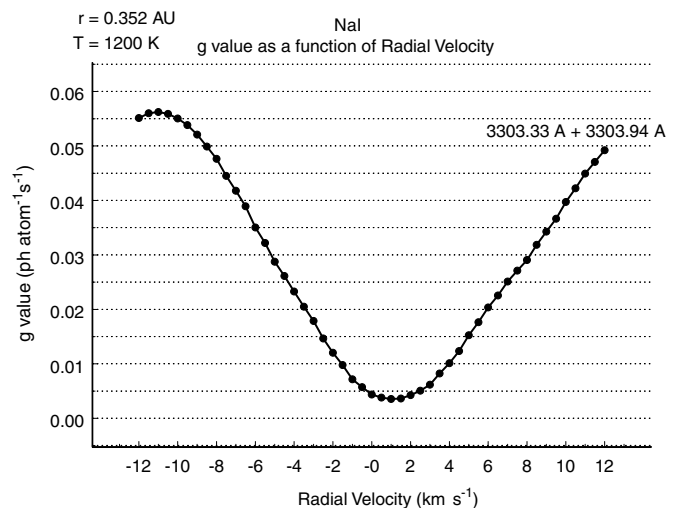


**Figure 6.** Combined  $g$  values are shown vs. heliocentric radial velocity for sodium emission lines at 3303.33 Å and 3303.94 Å for a temperature ( $T_g$ ) of 1200 K at a heliocentric radial distance of 0.352 AU. The individual lines have different radial velocity dependences.

the column abundances in Mercury's exosphere are expected to be above the limit at which  $\tau = 0.2$ . In fact, for line-of-sight column abundances expected, these lines will be quite optically thick and a scattering code or curve of growth analysis will be essential to the interpretation of abundance as a function of intensity.

Figure 1 shows  $g$  values for 12 species at 0.352 AU and a heliocentric relative velocity of  $-10$  km  $s^{-1}$ . For many of the species, this approaches the maximum  $g$  value. Exceptions are Mg I, Mg II, He I, O I, and OH. Figure 2 shows the variation of the  $g$  value with velocity for H Ly $\alpha$ . This and subsequent graphs were calculated for an orbital distance of 0.352 AU. Figure 3 shows the variation of  $g$  value with heliocentric radial velocity for the He 584 Å line. This line is not observable with the *MESSENGER* UVVS instrument, but will be observable with the *BepiColombo* UV spectrometer, PHEBUS. Figure 4 shows the  $g$  values for C I at the multiplet wavelengths <1560> Å and <1657> Å, co-added lines in a range smaller than 6 mÅ.

The gas temperature is high (12,000 K) because the carbon is assumed to be a product of exothermic dissociation. Figure 5 shows the  $g$  value for atomic oxygen. The value given is the total for the lines of the triplet. Figure 6 shows the total  $g$  value for the Na I doublet 3303.3 Å and 3303.9 Å. A temperature ( $T_g$ ) of 1200 K is consistent with ground-based observations of the width of the Na D lines (Potter & Killen 2008). The velocity dependence of the  $g$  value at the 3303.3 Å line is slightly asymmetric with respect to positive and negative radial velocity although the 3303.9 Å line is markedly asymmetric. Figure 7 shows the variation of the  $g$  value for the Na D doublet as a function of heliocentric radial velocity. The  $g$  value for the D1 line varies by about a factor of 10 from zero radial velocity to  $\pm 10$  km  $s^{-1}$ . Emission in the sodium D1 line is isotropic and unpolarized, but emission in D2 is both anisotropic and polarized (Chamberlain

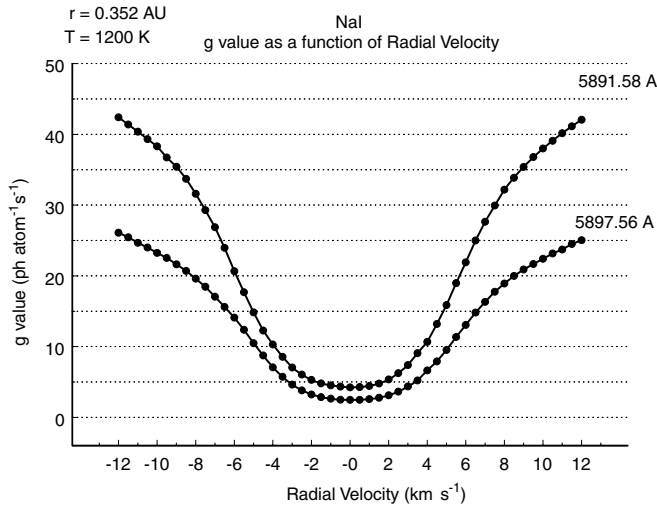
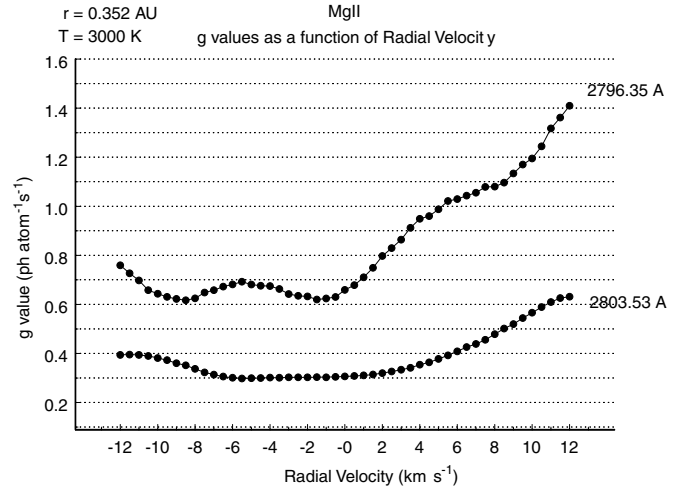


**Figure 7.** Variation of  $g$  values with heliocentric radial velocity for the sodium D doublet is given at a heliocentric distance of 0.352 AU and temperature ( $T_g$ ) of 1200 K, consistent with the line profile measured by Killen et al. (1999). The  $g$  value is a sharply varying function of radial velocity caused by the shape of the solar Fraunhofer absorption line.

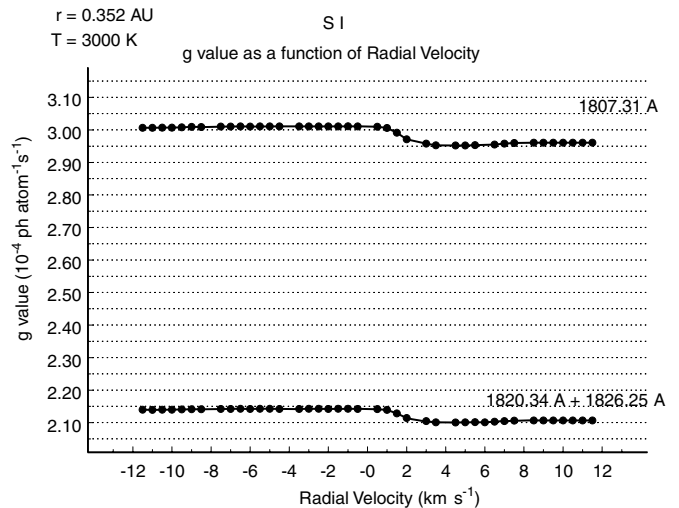
1961). The scattering phase function for D2 is

$$p(D_2, \theta) = 0.967 \cdot (1 + 0.102 \cdot \cos^2(\theta)), \quad (15)$$

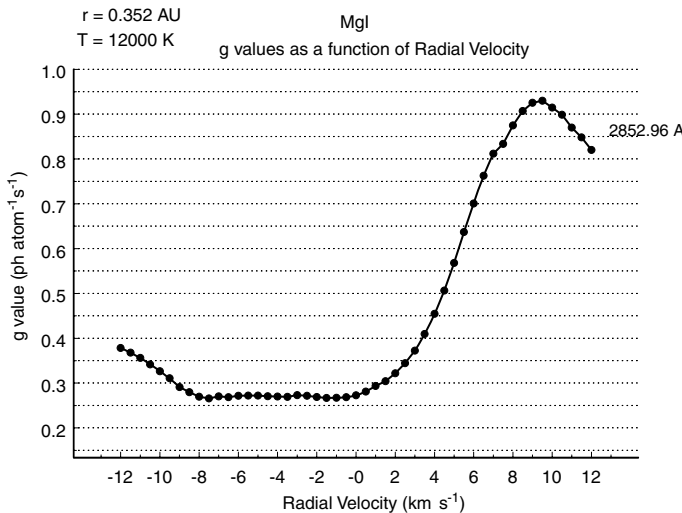
where  $\theta$  is the angle measured from the direction of incident light to the direction of scattered light. There is an approximate 10% difference in emission in the forward or backscattered direction and that at right angles to the incoming light. Figures 8 and 9 show that the  $g$  values are highly asymmetric with respect to positive and negative heliocentric radial velocity for the Mg I and Mg II lines in the near-UV at 2852.96, 2026 Å, and 2796, 2803 Å, respectively. In these cases, a positive radial velocity is more favorable for observations. A gas temperature of 12,000 K is associated with Mg I, whereas a temperature  $T_g = 3000$  K is assumed for Mg II as well as for S I, shown in Figure 10. There is almost no radial velocity dependence in  $g$  value for the S I 1807–1826 Å triplet, and the lines are quite weak. In this case, the negative radial velocity is the most favorable in which to observe but the advantage is modest. The  $g$  values for the



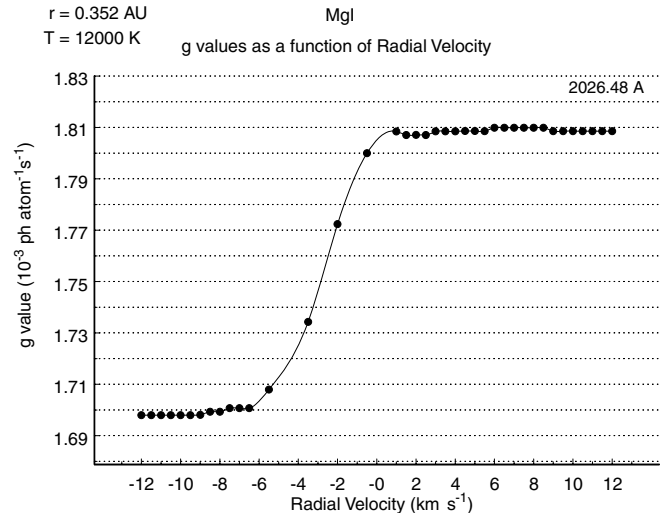
**Figure 9.**  $g$  value is shown as a function of radial velocity for the Mg II lines at 2796.35 and 2803.53 Å. The assumed temperature, 3000 K, would be consistent with an impact vaporization source.



**Figure 10.**  $g$  values are shown as a function of radial velocity for the sulfur triplet near 1807, 1820, and 1826 Å at a heliocentric distance of 0.352 AU and a temperature ( $T_g$ ) of 3000 K.



**Figure 8.**  $g$  values are shown as a function of radial velocity for Mg I at 2026.48 Å and 2852.96 Å. The strong asymmetry in this emission makes the positive radial velocity more favorable by a factor of 3 for the 2853 Å line.



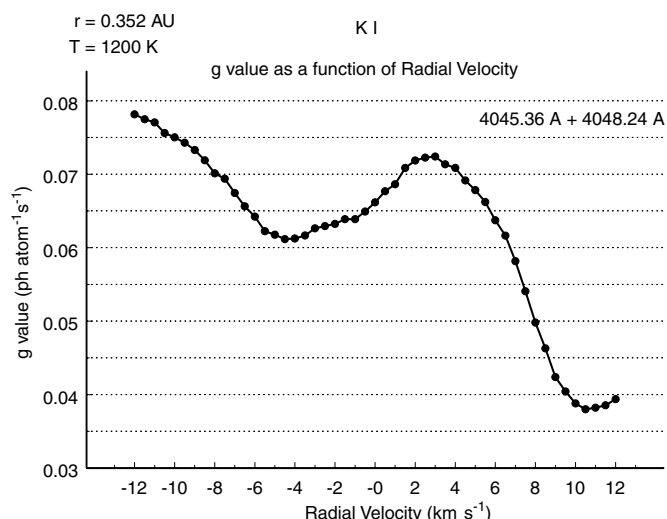
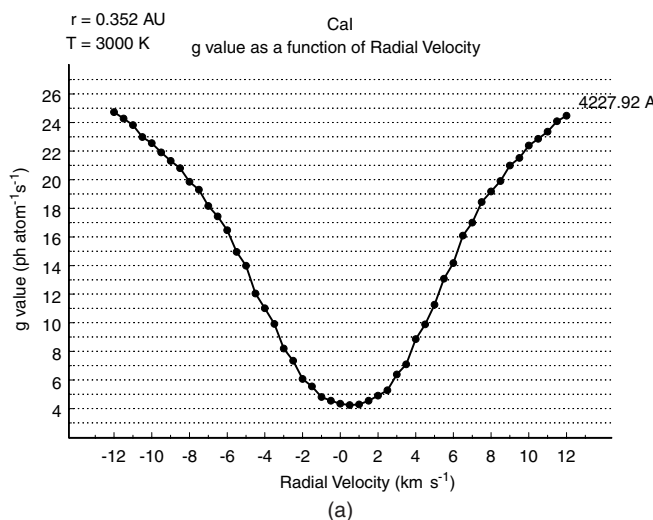


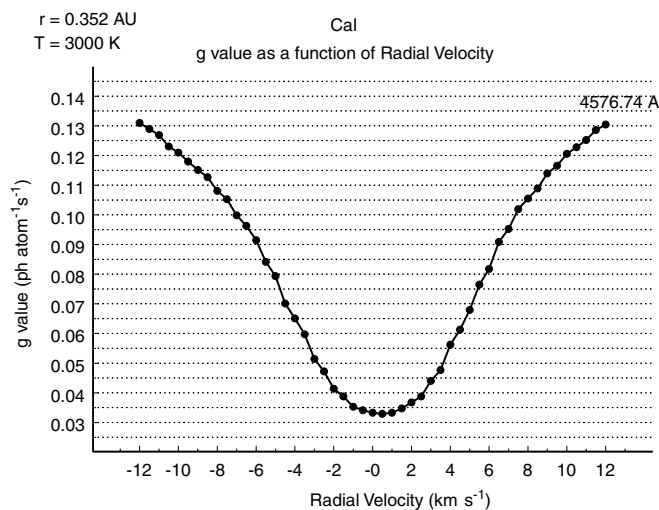
Figure 11.  $g$  values are given as a function of heliocentric radial velocity for the potassium 4045–4048 Å doublet is given at a heliocentric distance of 0.352 AU and temperature ( $T_g$ ) of 1200 K.

K I D doublet are larger by more than a factor of 2 for  $-12 \text{ km s}^{-1}$  radial velocity than for  $+12 \text{ km s}^{-1}$  radial velocity (Figure 11). This asymmetry makes observation more favorable for negative heliocentric radial velocity.  $g$  values are given for three Ca I lines (4227 Å, 4577 Å, and 2722 Å) in Figures 12(a), (b), and (c), respectively; the strongest line is at 4227 Å. The variation with heliocentric radial velocity is symmetric with positive and negative Doppler shift due to the broad solar Fraunhofer feature; a factor of 6 variation is indicated from zero Doppler shift to the maximum for the 4227 Å line. The 2722 Å line is narrower and shows a maximum  $g$  value at radial velocities of  $-7 \text{ km s}^{-1}$  and  $+9 \text{ km s}^{-1}$ . Figure 13 shows the radial velocity dependence of the  $g$  value for the Ca II doublet at 3935, 3969 Å. These lines, the strongest resonance lines of any ion in this spectral region, have a weak velocity dependence.

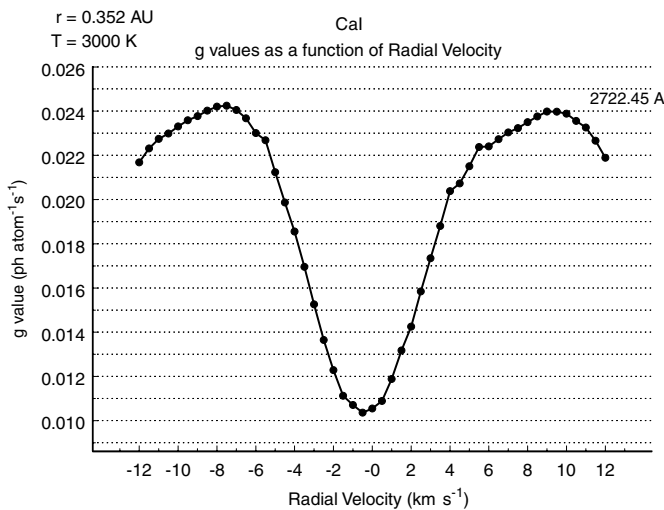
Figure 14 shows the  $g$  value for the OH band from 3070 Å to 3160 Å convolved with the MASC'S instrument function at five different values of radial velocity. Temperatures of 3000 K and 15,000 K were assumed. If OH has a significant nonthermal source component, rotation-vibration will be very different from a distribution starting out as thermal. The relaxation time, however, is quite short, so it is very unlikely that the properties



(a)



(b)



(c)

Figure 12. Strong variation of the Ca  $g$  values with radial velocity is given at a heliocentric distance of 0.352 AU and temperature ( $T_g$ ) of 3000 K. Observation at high Doppler shift yields a factor of 6 advantage in the 4227.92 Å line (a) and a factor of 4 in the 4576.74 Å line (b) and a factor of 2.4 in the 2722.45 Å line (c) over the rest emission at aphelion and perihelion.

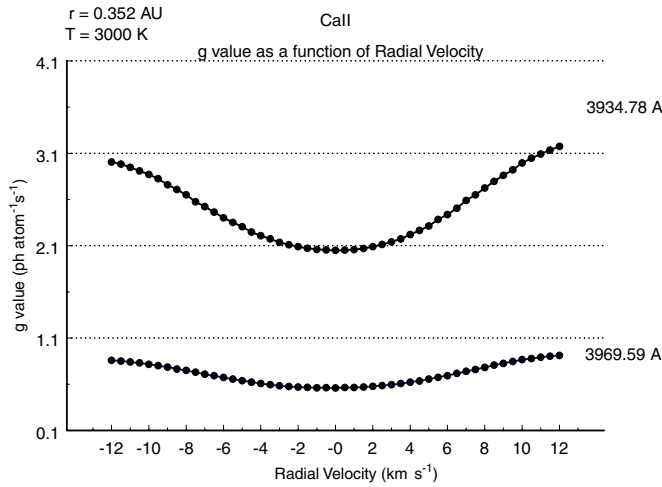


**Figure 13.** Ca II doublet at 3934, 3969 Å has the strongest  $g$  values of any ion in the spectral region considered herein. The variation with heliocentric radial velocity is fairly symmetric.

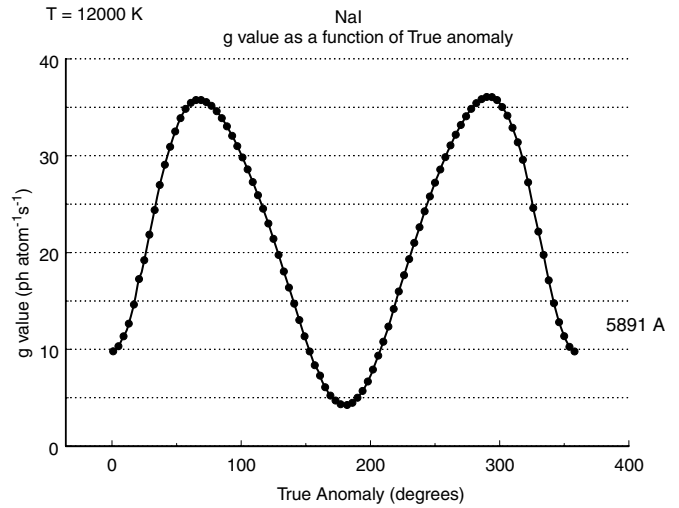


**Figure 15.** Sample plot of  $g$  value as a function of the true anomaly angle of Mercury for the Na 5891 Å line. The  $1/R^2$  variation with distance makes the true variation a double function of velocity, but a single function in true anomaly. Similar plots are shown for three other elements in Figures 16–18.

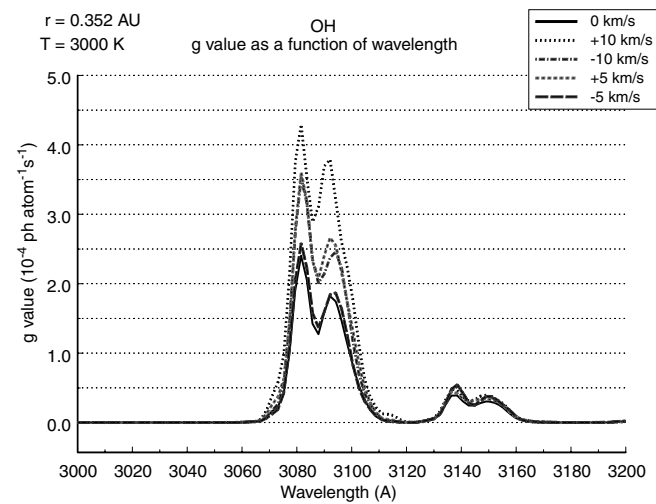
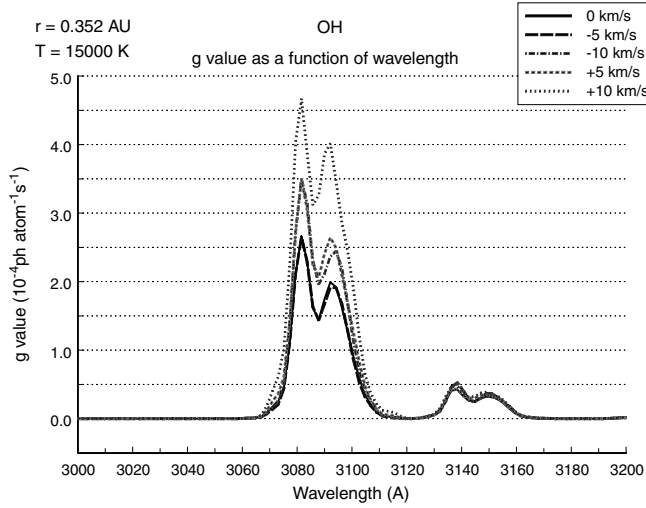


**Figure 14.**  $g$  value for OH combined with the MASCS instrument function is shown for five different radial velocities and at two temperatures: 15,000 K and 3000 K.

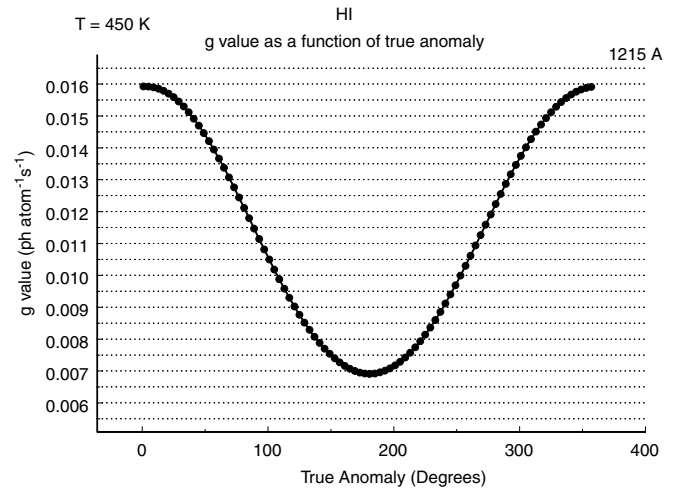


**Figure 16.** Sample plot of  $g$  value as a function of the true anomaly angle of Mercury for the case of the H I 1215 Å line.

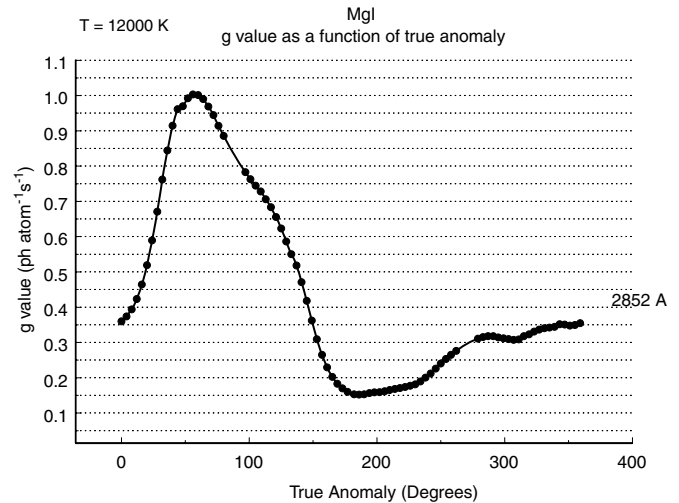


**Figure 17.** Sample plot of  $g$  value as a function of the true anomaly angle of Mercury for the case of the Mg I 2852 Å line.

of the excited dissociation product would be observed above the stabilized OH background. Figures 15–18 show the variations of  $g$  values with the true anomaly angle of Mercury for Na D2,

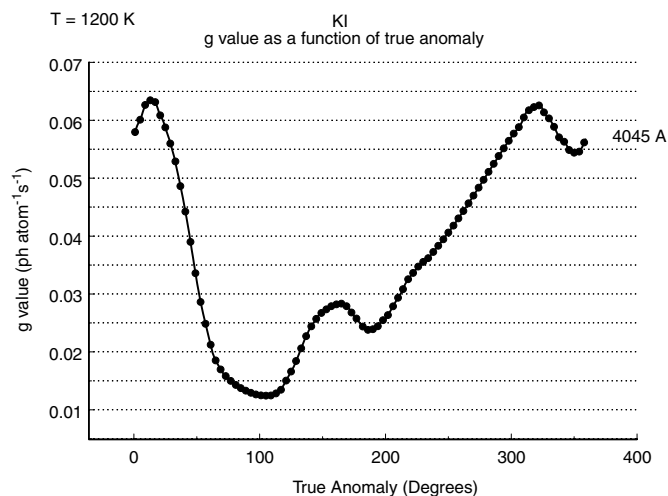


**Figure 18.** Sample plot of  $g$  value as a function of the true anomaly angle of Mercury for the case of the K I 4045 Å line.

H Ly $\alpha$ , Mg I 2852 Å, and K I 4045 Å. Note that the radial velocity variation is more important than the orbital distance in determining the  $g$ -value variation, except for H Ly $\alpha$  which has little radial velocity dependence. The  $g$  values are highly asymmetric with respect to outbound (positive radial velocity) and inbound (negative radial velocity) legs of the orbit for Mg I (Figure 17) and K I (Figure 18).

R.K. and N.M. were supported by NASA under the *MESSENGER* Participating Scientist Program, grant NNX07AR78G.

APPENDIX

**Table A1**  
Solar flux model from 30–200 Angstroms

Wavelength (Å)	Differential Flux (photons/cm <sup>2</sup> /s/Å)	Record
.3000000E+03	.742700E+08	(calculated)
.3000020E+03	.742700E+08	(calculated)
.3000040E+03	.742700E+08	(calculated)
.3000060E+03	.742700E+08	(calculated)
.3000080E+03	.742700E+08	(calculated)

(This table is available in its entirety in a machine-readable form in the online journal. A portion is shown here for guidance regarding its form and content.)

**Table A2**  
Solar flux model from 200–1300 Angstroms

Wavelength (Å)	Differential Flux (photons/cm <sup>2</sup> /s/Å)	Record
.2000000E+04	.691500E+11	(calculated)
.2000005E+04	.691500E+11	(calculated)
.2000010E+04	.691500E+11	(calculated)
.2000015E+04	.691500E+11	(calculated)
.2000020E+04	.691500E+11	(calculated)

(This table is available in its entirety in a machine-readable form in the online journal. A portion is shown here for guidance regarding its form and content.)

REFERENCES

Bates, D. R., & Damgaard, A. 1949, *Phil. Trans. R. Soc. A*, **242**, 101  
 Broadfoot, A. L., Shemansky, D. E., & Kumar, S. 1976, *Geophys. Res. Lett.*, **3**, 577  
 Brown, R. A., & Yung, Y. L. 1976, in Jupiter, ed. Tom Gehrels, M. S. Matthews (Tucson, AZ: Univ. Arizona Press) 1102  
 Chamberlain, J. W. 1961, *Physics of the Aurora and Airglow* (New York: Academic)  
 Chassefiere, E., & The PHEBUS Team, 2009, *Planet. Space Sci.*, doi:10.1016/j.pss.2008.05.018  
 Condon, E. U., & Shortley, G. H. 1959, *Theory of Atomic Spectra* (Cambridge: Cambridge Univ. Press), 441  
 Elliot, A. J., Chenier, M. P., & Ouellett, D. C. 1990, *Can. J. Chem.*, **68**, 712  
 Killen, R. M., Bida, T., & Morgan, T. H. 2005, *Icarus*, **173**, 300  
 Killen, R. M., Potter, A. E., Fitzsimmons, A., & Morgan, T. H. 1999, *Planet. Space Sci.*, **47**, 1449  
 Klarsfeld, S. 1988, *J. Phys. B: At. Mol. Opt. Phys.*, **21**, L717  
 Mitchell, A. C. G., & Zemansky, M. W. 1971, *Resonance Radiation and Excited Atoms* (Cambridge: Cambridge Univ. Press) Lib. Cong. A62-5588  
 McClintock, W. E., & Lankton, M. R. 2007, *Space Sci. Rev.*, **131**, 481  
 Potter, A. E., & Killen, R. M. 2008, *Icarus*, **194**, 1  
 Potter, A. E., Killen, R. M., & Morgan, T. H. 2007, *Icarus*, **186**, 571  
 Ralchenko, Yu., Kramida, A. E., Reader, J., & The NIST ASD Team, 2008, in *NIST Atomic Spectra Database* (Gaithersburg, MD: National Institute of Standards and Technology)  
 Shemansky, D. E. 1980, *ApJ*, **236**, 1043  
 Shemansky, D. E., & Smith, G. R. 1981, *J. Geophys. Res.*, **86**, 9179  
 Snow, M., & The LISIRD Team, 2005, *EOS Trans. AGU*, **86** (52), Fall Meeting Suppl. Abstract IN-33B-1180  
 Wurz, P., Rohner, U., Whitby, J. A., Kolb, C., Lammer, H., Dobnikar, P., & Martin-Fernandez, J. A. 2007, *Icarus*, **191**, 486